Journal of Biomechanical Science and Engineering

Vol. 6, No. 4, 2011

Numerical Study on the Morphology and Mechanical Role of Healthy and Osteoporotic Vertebral Trabecular Bone*

Yuto YOSHIWARA**, Miguel CLANCHE***, Khairul Salleh BASARUDDIN**, Naoki TAKANO**** and Takayoshi NAKANO*****

**Graduate School of Science and Technology, Keio University,
3-14-1 Hiyoshi, Kohoku-ku, Yokohama, Kanagawa 223-8522, Japan
E-mail: yoshiwara@z2.keio.jp

***Ecole Centrale de Nantes, 1, rue de la Noe 44300 Nantes, France

****Department of Mechanical Engineering, Keio University,
3-14-1 Hiyoshi, Kohoku-ku, Yokohama, Kanagawa 223-8522, Japan

*****Division of Materials and Manufacturing Science, Graduate School of Engineering, Osaka University,
2-1, Yamadaoka, Suita, Osaka 565-0871, Japan

Abstract

This study presents a numerical methodology to clarify the morphology of complex trabecular network architecture in human lumbar vertebra by means of the new post-processing technique for calculated microscopic stress by the homogenization method. Micro-CT image-based modeling technique is used and careful but intuitive and easy-to-use method for microstructure model, in other words region of interest (ROI), is also presented. The macroscopic homogenized properties that include not only the Young's moduli but also shear moduli could explain the difference of morphology between healthy and osteoporotic bones. This paper focuses on the change of degree of anisotropy. Then, the microscopic stress under three basis load cases was analyzed. In this analysis, the homogenization method has a merit in the computational cost. The trabeculae are classified into eight groups from the viewpoint of load bearing function against three loading conditions in the proposed post-processing of numerical results. It contributes to the understanding of the mechanical role of trabecular bone in vertebra. The primary trabecular bone that has been supposed to support the self-weight and secondary bone that connects the primary bone are successfully visualized. The discussion on the mechanical role of plate-like trabecular bone in the load path network system is also highlighted.

Key words: Vertebra, Trabecular Bone, Numerical Analysis, Homogenization Method, Microsccopic Stress

1. Introduction

Diagnosis of osteoporosis has been performed by using DEXA method, which is a noninvasive and an affordable and easy method for the diagnosis of osteoporosis[1]. In addition, the observation of stress[2-3] and morphology[4] of trabeculae in microscopic scale is expected to provide a better understanding of osteoporosis. The numerical biomechanical studies such as the mechanism of remodeling of human bone[5-7] have implied that the shape resulting from this continual reconstruction seemed to be optimized against external stimuli.

One of the authors has measured the crystallite orientation of biological apatite (BAp) by X-ray diffraction method and found the correlation of the preferential alignment of BAp

*Received 7 Dec., 2010 (No. 10-0593)
[DOI: 10.1299/jbse.6.270]

and the mechanical loading conditions[8-9]. Hence, the authors have proposed a multiscale analysis methodology that bridges nanoscale BAp crystallite orientation, microscale trabecular architecture and macroscopic properties[10-11]. It was advantageous over other past numerical studies because they have used isotropic constitutive law for bone[5-6]. While the authors' multiscale analysis employed anisotropic material model for trabecular bone resulting from preferential alignment of c-axis of BAp crystallite. The homogenization theory[12-14] was used for this multiscale analysis with micro-CT image-based modeling[15].

The homogenization theory can predict both macroscopic properties based on the microstructure and microscopic response under macroscopic boundary condition. Relations between bone density and Young's modulus have been described by Keyak[16], Keller[17] or Carter[18], as a result of experiments. In this paper, the calculated macroscopic Young's modulus is compared with the empirical equation of Keyak for verification. Then, not only macroscopic Young's moduli but also shear moduli are investigated to discuss the differences in morphology of healthy and osteoporotic bone. By virtue of the characteristic of the homogenization theory, the post-processing technique is proposed to study the mechanical role of trabecular bone under variety of loading conditions.

It is well known that the trabecular bone consists of plate-like and rod-like bone. Also, it is known that primary trabecular bone exists almost parallel to the axial direction that supports the self-weight. On the other hand, the rod-like trabecular bone perpendicular to the axial direction, i.e., left-right and posterior-anterior directions, is regarded as secondary trabecular bone. In this paper, morphological study focuses on the mechanical role of trabecular bone highlighting the primary and secondary bone as well as plate-like bone.

In the following chapter, the overview of the image-based modeling, homogenization theory, modeling of region of interest (ROI) and the post-processing technique are described. Note that ROI is a popular term in biomechanics field, which is equivalent to the unit cell or RVE (representative volume element) in the homogenization method. In chapter 3, the calculated macroscopic properties and evaluation of microscopic stress are shown. Then, the morphology and mechanical role of trabecular bone is discussed.

2. Materials and Methods

2.1 Materials and image-based modeling

The three-dimensional voxel model has been reconstructed from hundreds of micro-CT images of trabecular bone in fourth lumbar of human vertebra. Two subjects are studied in this paper. From DEXA analysis, the one is supposed to be healthy (male; age 68 years), whilst the other osteoporotic (female; age 86 years). A micro-CT device (SMX-100CT, Shimadzu, Kyoto, Japan) was used to examine the bone specimens in this studied. The specimens were scanned using a voltage of 40 kV and a current of 30 μA. The resolution of micro-CT images is 31.91 μm for healthy bone and 29.92 μm for osteoporotic bone. They are used only for geometrical modeling. Binarization, three-dimensional reconstruction of the solid and voxel finite element meshing were carried out. The voxel finite element size is equal to the micro-CT image resolution using the authors' original software DoctorBQ[19] in order to avoid the discussion of numerical accuracy depending on the element size.

The overall process flow of this study can be summarized in Fig. 1. The number in the bracket in Fig.1 indicates the section where each process is described. The Young's moduli at microscale have been set as in Fig. 1, whilst the Poisson's ratio were determined as ν_{31}= ν_{32}= ν_{12}= ν_{21}=0.4 and ν_{13}= ν_{23}=0.2 to hold the symmetry of the elastic tensor. The material axis-3 corresponds to c-axis of BAp crystallite. The shear moduli were assumed as isotropic with G_{23}=G_{31}=G_{12}=1.8 GPa. See Appendix A for the setup of anisotropic material axes. The application of the homogenization theory, ROI extraction, load conditions, calculation of microscopic stress and post-processing technique in the flowchart are in the following.

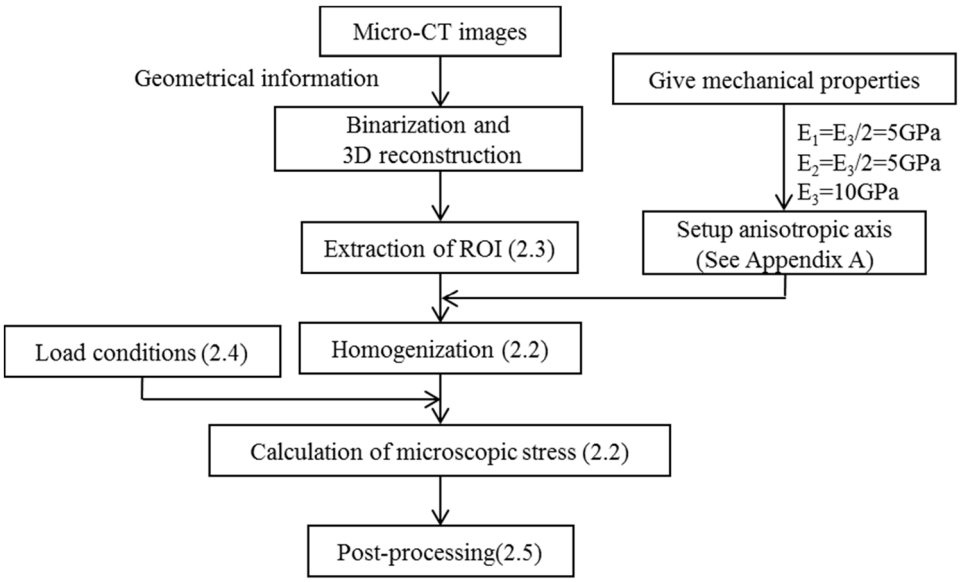

Fig. 1 The process flow of this study

2.2 Homogenization theory

This is a multiscale theory of mechanics for arbitrary heterogeneous media and the derived partial differential equations are solvable using finite element method[12-14]. It was firstly developed for materials with periodic microstructures, but one of the authors have proved the accuracy even for materials with random microstructures by comparison with experimental results for porous alumina[20] and porous titanium[21].

The microscopic equation in Eq. (1) is analyzed for microstructure model with periodic boundary condition, where $\boldsymbol{D}$ is the elastic tensor which takes into account the crystallite orientation of BAp[10-11].

$$\int_Y D_{ijmn}\frac{\partial \chi_m^{kl}}{\partial y_n}\frac{\partial \delta u_i^1}{\partial y_j}dY = \int_Y D_{ijkl}\frac{\partial \delta u_i^1}{\partial y_j}dY \quad \forall \delta u_i^1 \tag{1}$$

χ, which is a periodic function with respect to the microstructure, is the characteristic displacement that represents the microscopic perturbation of displacement due to the heterogeneity. Once the characteristic displacement is obtained, the macroscopic homogenized elastic tensor is calculated by Eq. (2).

$$D_{ijkl}^H = \frac{1}{|Y|}\int_Y \left(D_{ijkl} - D_{ijmn}\frac{\partial \chi_m^{kl}}{\partial y_n} \right) dY \tag{2}$$

where $\boldsymbol{D^H}$ is homogenized macro-properties, Y is the region of the microstructure model and $|Y|$ is the volume of microstructure model. Then, the macroscopic equation, Eq. (3), coincides with the classical micromechanics theory.

$$\int_\Omega D_{ijkl}^H \frac{\partial u_k^0}{\partial x_l}\frac{\partial \delta u_i^0}{\partial x_j}d\Omega = \int_\Gamma t_i \delta u_i^0 d\Gamma \quad \forall \delta u_i^0 \tag{3}$$

$\boldsymbol{t}$ denotes the traction applied on the surface Γ of domain Ω.

The merit of this theory lies in the capability of calculating the microscopic response. The microscopic stress $\boldsymbol{\sigma}$ can be obtained by Eq. (4), where $\mathbf{E}$ denotes macroscopic strain and macroscopic stress $\boldsymbol{\Sigma}$.

$$\sigma_{ij} = \left(D_{ijkl} - D_{ijmn}\frac{\partial \chi_m^{kl}}{\partial y_n} \right) E_{kl} = \left(D_{ijkl} - D_{ijmn}\frac{\partial \chi_m^{kl}}{\partial y_n} \right) \left(D_{klpq}^H \right)^{-1} \Sigma_{pq} \tag{4}$$

The consistency between microscopic and macroscopic behaviors is assured because Eq. (5) holds.

$$\Sigma = <\sigma> = <D><\varepsilon> = D^H : \mathbf{E} \tag{5}$$

Here < > indicates the volumetric averaging operator.

Note here that, in solving the microscopic equation, Eq. (1), for osteoporotic trabecular bone with very low bone density, the periodic boundary condition is hardly assigned. In such a ill-conditioned problem, one of the authors has proposed to use wrapping element layer for the microstructure model to obtain accurate solution[19].

In this analysis, most of the computational time is spent for solving microscopic equation. One of the reasons is that the number of voxel finite elements is large and element-by-element SCG (scaled conjugate gradient) method, which is one of the iterative equation solvers, is used. Especially, when the BAp orientation is considered, the convergence of SCG solver becomes extremely slow. However, once the microscopic equation is solved, the microscopic stress in Eq. (4) can be calculated very easily for variety of macroscopic stress condition in Eq. (6).

$$\Sigma_{ij} = \left\lfloor \Sigma_{11} \quad \Sigma_{22} \quad \Sigma_{33} \quad \Sigma_{23} \quad \Sigma_{31} \quad \Sigma_{12} \right\rfloor^T \tag{6}$$

2.3 Regions of interest (ROI)

Figure 2 shows the location of four ROIs for healthy bone. In this paper, left-right axis is defined as axis-1, posterior-anterior axis is defined as axis-2, and craniocaudal axis in vertical direction is defined as axis-3. The correlation between this axis setup and human body is described in Appendix B. ROI No. 1 has been selected as large as possible from micro-CT image. Meanwhile, ROI No. 2 to No. 4 are local models representing plate-like and rod-like trabecular bone rich regions respectively. Note that plate-like and rod-like trabecular bones are seen in healthy vertebral bone as shown in Appendix C. Large ROI No.1 will represent the overall characteristics best, and also contain the load paths in the trabecular bone studied later rather than small ROIs. Comparisons are made between large ROI and small ROIs in this paper. Specification for each ROI is shown in Table 1. For osteoporotic bone, one ROI in Fig. 3 has been chosen where the dimension is almost same with ROI No. 1, as listed in Table 1. As was shown in Appendix C, small ROI in plate-like trabecular bone rich region was hardly extracted from osteoporotic bone. Hence, only large ROI was chosen.

In the above selection of ROIs, the distribution of areal bone density[22] was carefully investigated as shown typically in Fig. 4. Now, the areal bone density is calculated by Eq. (7) [22]. For comparison, the standard definition of volumetric bone density (simply expressed as bone density) is also shown in Eq. (7).

$$\left.\begin{aligned} \text{Areal bone density} &= \frac{1}{A}\int \rho dA \\ \text{Volumetric bone density} &= \frac{1}{V}\int \rho dV \end{aligned}\right\} \quad \left(\rho = \begin{cases} 1 \text{ for trabecular} \\ 0 \text{ for marrow} \end{cases}\right) \tag{7}$$

where A is the cross-sectional area of the selected ROI and V is its volume. Fig. 4 is the screen copy of the authors' original software DoctorBQ[19]. The green line displays the volumetric bone density of the ROI, which is 17.2% in the case of ROI No. 1. In other words, the green line is the average of oscillating areal bone density theoretically. As shown in Fig. 4, this holds reasonably for this ROI. Otherwise, the homogenization fails. Besides, the areal bone density at the both boundaries must be almost same to assure the periodicity condition in the homogenization analysis. This is always necessary to avoid the numerical error by assuming the periodicity condition. The slight difference in ROI location will affect much to the numerical result. Consequently , Fig. 4 is very helpful to extract appropriate

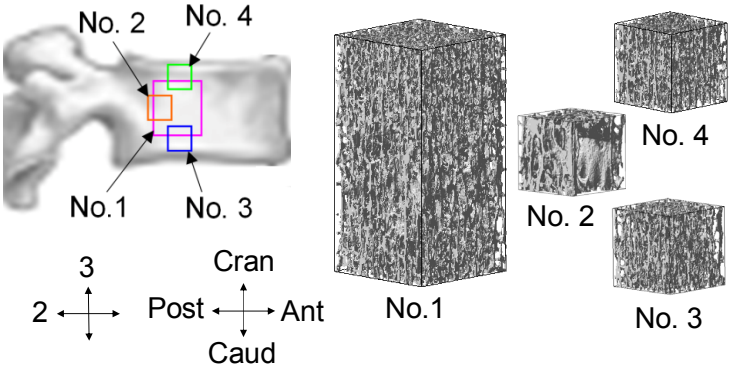

Fig. 2 ROIs for healthy bone

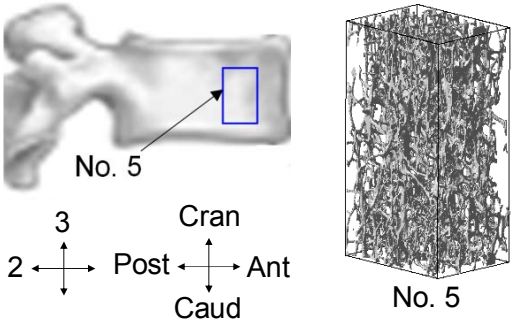

Fig. 3 ROIs for osteoporotic bone

Table 1 Specification of ROIs

	No.	ROI size (mm^3)	Bone density (%)	Number of voxels
Healthy	1	6×6×12	17.2	2,781,416
	2	4×4×4	17.7	353,521
	3	4×4×4	15.9	382,122
	4	4×4×4	16.9	406,477
Osteoporosis	5	5×6.6×12	6.04	877,277

ROI for homogenization[11]. The left hand side figures showing the cross section corresponds to the red marked location in the graph of areal bone density.

For ROI No.5 that was extracted from osteoporotic bone, the distribution of the areal bone density was examined in the same way. The reasonable definition of the average and the condition to assure periodicity were confirmed. In addition, ROI No.5 has wrapping element layer[19] as described in 2.2.

2.4 Load conditions

In this paper, three compressive load cases expressed by macroscopic stress as Eq. (8) are analyzed and discussed. Then, variety of load cases can be easily analyzed by linear combination of three unit load cases, if requested.

$$\left.\begin{aligned}\Sigma_1 &= \lfloor -1 \quad 0 \quad 0 \quad 0 \quad 0 \quad 0 \rfloor^T \\ \Sigma_2 &= \lfloor 0 \quad -1 \quad 0 \quad 0 \quad 0 \quad 0 \rfloor^T \\ \Sigma_3 &= \lfloor 0 \quad 0 \quad -1 \quad 0 \quad 0 \quad 0 \rfloor^T\end{aligned}\right\} \tag{8}$$

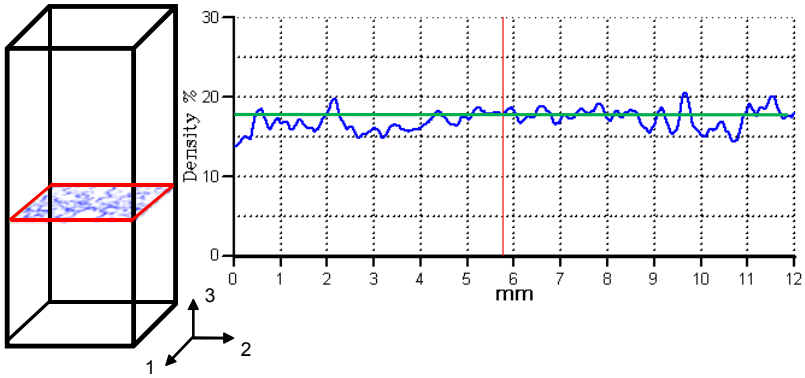

(a) Density distribution along craniocaudal direction

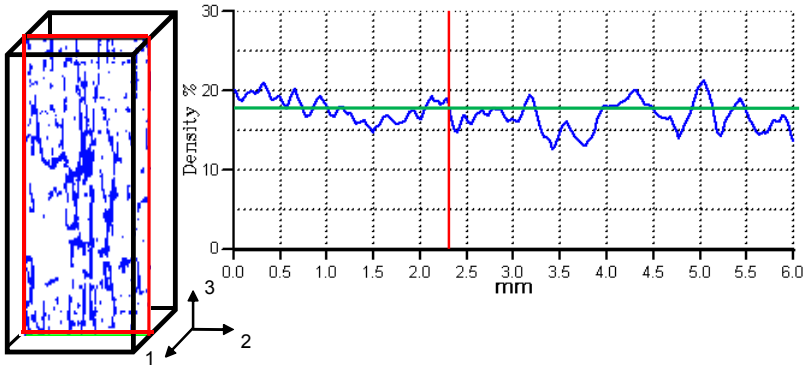

(b) Density distribution along left-right direction

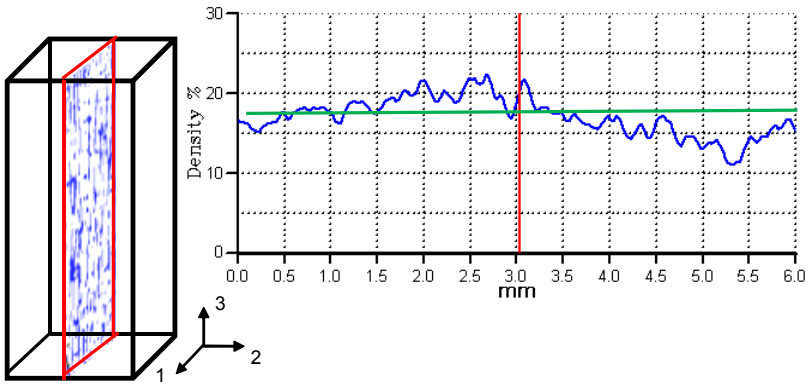

(c) Density distribution along anterior-posterior direction

Fig. 4 Morphology analysis for ROI modeling in case of No. 1

2.5 Post-processing of microscopic stress

The main purpose of this paper lies in the understanding of mechanical role of each portion in trabecular bone under various macroscopic loading cases. In pursuit of this, the region where higher microscopic stress than its average appears is supposed to work as the main load path, and it is extracted using the histogram of microscopic principal stress as shown in Fig. 5(a) and (b). This approach is formulated in Eq. (4), which implies that higher microscopic stress contributes to the increase of macroscopic stiffness under certain constant macroscopic strain. Here, for each voxel element, absolute value of maximum principal stress and that of minimum principal stress are compared. Then, the bigger one is adopted as the principal stress for that element in this paper. Repeating this post-processing

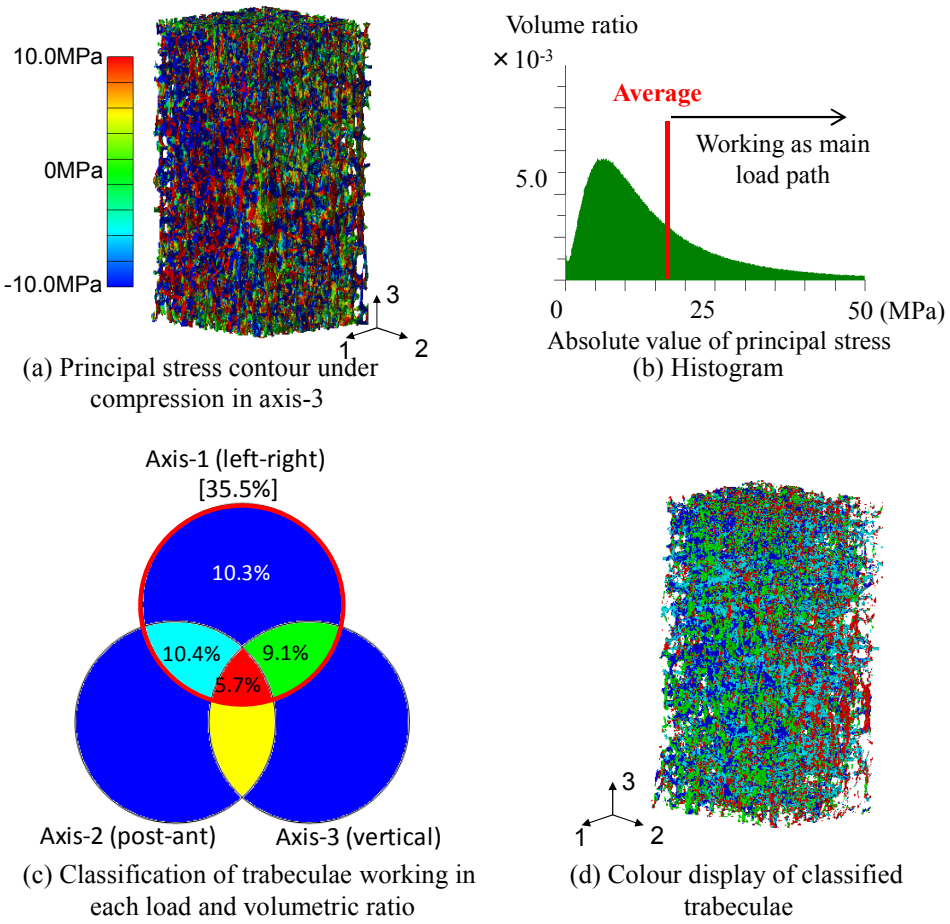

(a) Principal stress contour under compression in axis-3

(b) Histogram

(c) Classification of trabeculae working in each load and volumetric ratio

(d) Colour display of classified trabeculae

Fig. 5 Schematic of post-processing in case of ROI No.1

for various loading cases, the trabeculae can be classified to their respective load bearing capability. If three compressive load cases in axes-1, 2 and 3 as shown in Eq. (8) are considered, the above post-processing yields the Venn diagram as shown in Fig. 5(c). The volumetric ratio for each classified function can easily be counted. The percentage in [ ] indicates the ratio of the number of voxel corresponding to the total number of voxels working under one load case. Finally, Fig. 5(d) displays the mechanical role of trabecular bone under the compressive load in axis-1, for instance. The colors in Fig. 5(d) correspond to the colors of classified trabeculae indicated in Venn diagram as shown in Fig. 5(c). This helps the understanding of complicated trabecular morphology as well as the load path network.

3. Results

3.1 Homogenized properties

Homogenized elastic tensor has been calculated for four ROIs of healthy bone and one ROI of osteoporotic bone. The orthotropic material model was reasonably applied without any rotation of axes for all ROIs.

The calculated Young's moduli in Fig. 6 were compared with experimental results performed by Keyak et al.[16]. The error bar indicates the bounds of experimental results with respect to the bone density. Although Keyak et al.[16] has obtained the regression equation for Young modulus in vertical direction as $E = 33900\rho^{2.2}$, the original experimental results show surprisingly big scattering. The regression line is almost the average of dispersion

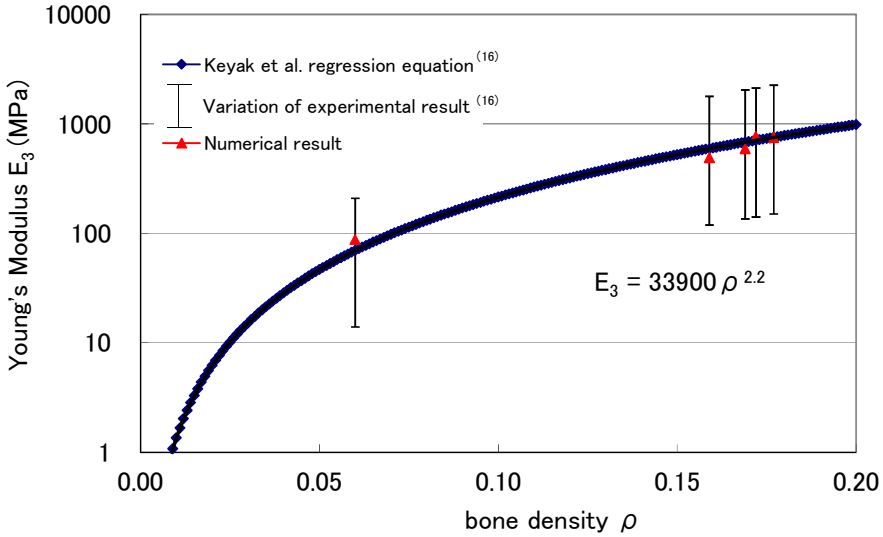

Fig. 6 Comparison between numerical and Keyak's model

Table 2 Homogenized properties for all ROIs
(a) Young's Moduli

	No.	Bone Density (%)	E_1 (MPa)	E_2 (MPa)	E_3 (MPa)	E_1/E_3	E_2/E_3
Healthy	1	17.2	58.5	67.2	765.0	0.077	0.088
	2	17.7	80.9	73.7	746.3	0.108	0.099
	3	15.9	25.4	33.0	490.5	0.052	0.067
	4	16.9	40.7	37.6	592.7	0.069	0.063
Osteoporosis	5	6.04	1.2	6.5	87.9	0.014	0.074

(b) Shear Moduli

	No.	Bone Density (%)	G_{12} (MPa)	G_{23} (MPa)	G_{31} (MPa)	G_{23}/G_{12}	G_{31}/G_{12}
Healthy	1	17.2	20.21	51.58	46.16	1.95	2.03
	2	17.7	22.93	64.51	53.15	2.35	2.36
	3	15.9	13.71	26.69	27.77	2.81	2.32
	4	16.9	13.85	32.53	32.73	2.55	2.28
Osteoporosis	5	6.04	0.46	4.08	2.55	4.48	3.52

of the experimental results. Good agreement to this line proves the reliability of numerical model.

All Young's moduli are presented in Table 2(a) with bone density and ratio to Young's modulus in vertical axis. In the same manner, shear moduli are in Table 2(b). For healthy bone, homogenized Young's moduli are almost isotropic between axis-1 (right-left) and axis-2 (posterior-anterior). But they are only approximately 8% of Young's modulus in axis-3 in case of ROI No.1. The difference among four ROIs is discussed later. For osteoporotic bone, Young's moduli show anisotropy since that in axis-1 is approximately 1/5 of that in axis-2 and thus only 1% of that in axis-3.

3.2 Evaluation of microscopic stress

Venn diagrams are shown in Fig. 7 for ROIs No. 1, 2, 4 and 5, because those for No. 3 and No. 4 are almost same. Among three ROIs of healthy bone (No. 1, 2 and 4), the percentages in Venn diagrams were similar between No. 1 (large ROI) and No. 2 (plate-like

trabeculae rich). However, for No. 4 (rod-like trabeculae rich), the percentage under vertical compressive load was lower than the others. Hence, the overall behavior is close to that in plate-like trabeculae rich region but the rod-like trabeculae rich region near the intervertebral discs show different mechanical response. In case of osteoporotic bone, the percentage under vertical compressive load was lower than the healthy case. Also, that under loading in axis-1 was slightly lower than that in axis-2, which corresponds to the macroscopic properties shown in Table 1(a).

The above classification was visualized as shown in Fig. 8 for ROI No.1 of healthy bone and in Fig. 9 for ROI No. 5 of osteoporotic bone. In Fig. 8(c) and Fig. 9(c), trabeculae working as a main load path under vertical compressive load are highlighted. As is more clearly seen in the magnified view of a certain portion, they are supposed to be the so called primary trabecular bone. Here, the maximum principal stress in red always has positive value, while the minimum principal stress in blue negative value. Compare with the original 3D model in Fig. 8(a) and Fig. 9(a), the complicated network architecture was successfully simplified from the mechanical point of view.

On the other hand, Fig. 10 shows the classified result under non-vertical load cases. They are totally different from Figs. 8 and 9. Careful observation by magnified view, which is typically shown in Fig. 10, tells us the secondary trabecular bone is successfully highlighted.

The plate-like trabecular bone included in ROI No. 2 is shown in Fig. 11. The classification of the mechanical role is visualized from Fig. 11(b) to Fig. 11(d). Yellow part is the typical plate-like bone, which supports the loads in vertical and post-ant directions only. The simplified morphology of ROI No.2 consisting of plate-like trabecular bone and connecting rod-like trabecular bones are illustrated in Fig. 11(e). Now also see Appendix C.

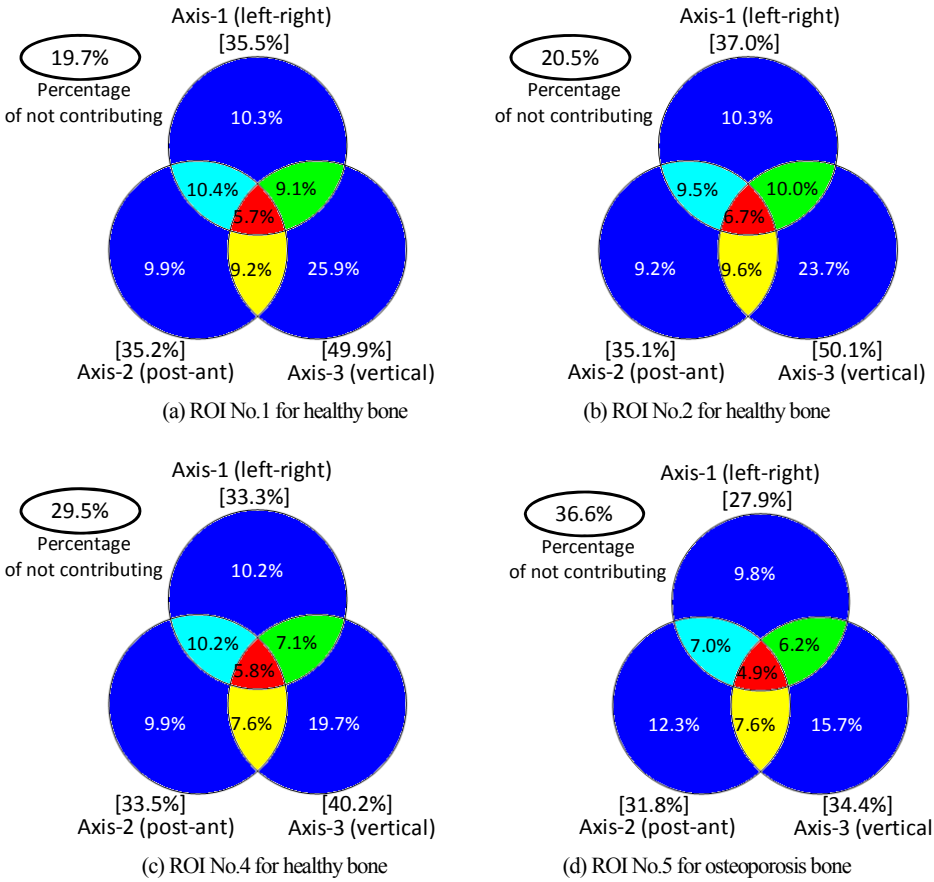

(a) ROI No.1 for healthy bone

(b) ROI No.2 for healthy bone

(c) ROI No.4 for healthy bone

(d) ROI No.5 for osteoporosis bone

Fig. 7 Volumetric ratio of trabeculae working under three uni-axial compression loads

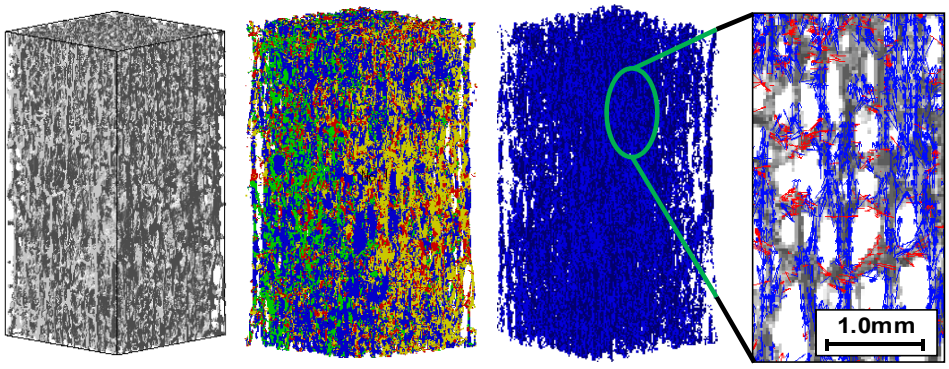

(a) Original 3D model (b) Classified trabecular (c) Primary trabeculae

Fig. 8 Trabeculae working under compression in axis-3 and highlighted view of primary trabeculae in healthy bone

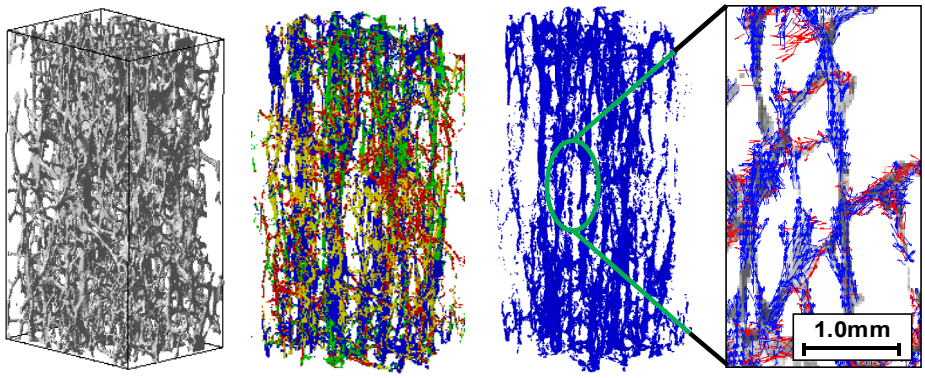

(a) Original 3D model (b) Classified trabecular (c) Primary trabeculae

Fig. 9 Trabeculae working under compression in axis-3 and highlighted view of primary trabeculae in osteoporotic bone

The load path transmissions in the plate-like and rod-like trabecular bones are illustratively shown in Fig. 11(e). Suppose that the plate-like trabecular bone is subjected to compressive load in axis-3 as indicated in black double-end arrows. The load coming into the plate-like bone is transmitted not only to the connecting rod-like bone in axis-3 but also to the connecting rod-like bones in axis-2 as displayed in black single-end arrows. The similar pattern of load path transmission occurred when the loads applied in axis-2 as displayed in brown double-end arrows, where it can be seen that the some part of the applied load is transmitted to axis-3, as illustrated in brown single-end arrows.

4. Discussion

4.1 Anisotropy of osteoporotic trabecular bone

The Young's modulus in left-right direction was lower than that in post-ant direction as shown in Table 2(a). By careful observation of the trabecular bone, stiff enough trabeculae in post-ant direction were found, which contributed to keep the same ratio E_2/E_3 with healthy bone.

The shear moduli with respect to the axial direction for healthy bone are doubly higher than that in horizontal plane perpendicular to axial direction as shown in Table 2(b). While, the shear modulus G_{31} (axis-1 is in left-right direction) for osteoporotic bone is again lower than G_{23} (axis-2 is in post-ant direction) in the same manner with Young's modulus. Note that they are still higher than G_{12}, and the ratio to G_{12} is larger for osteoporotic bone than healthy bone. This means the degree of anisotropy increases for osteoporotic bone. In other words, the decrease of stiffness in left-right and post-ant directions is larger than the decrease of stiffness in axial direction.

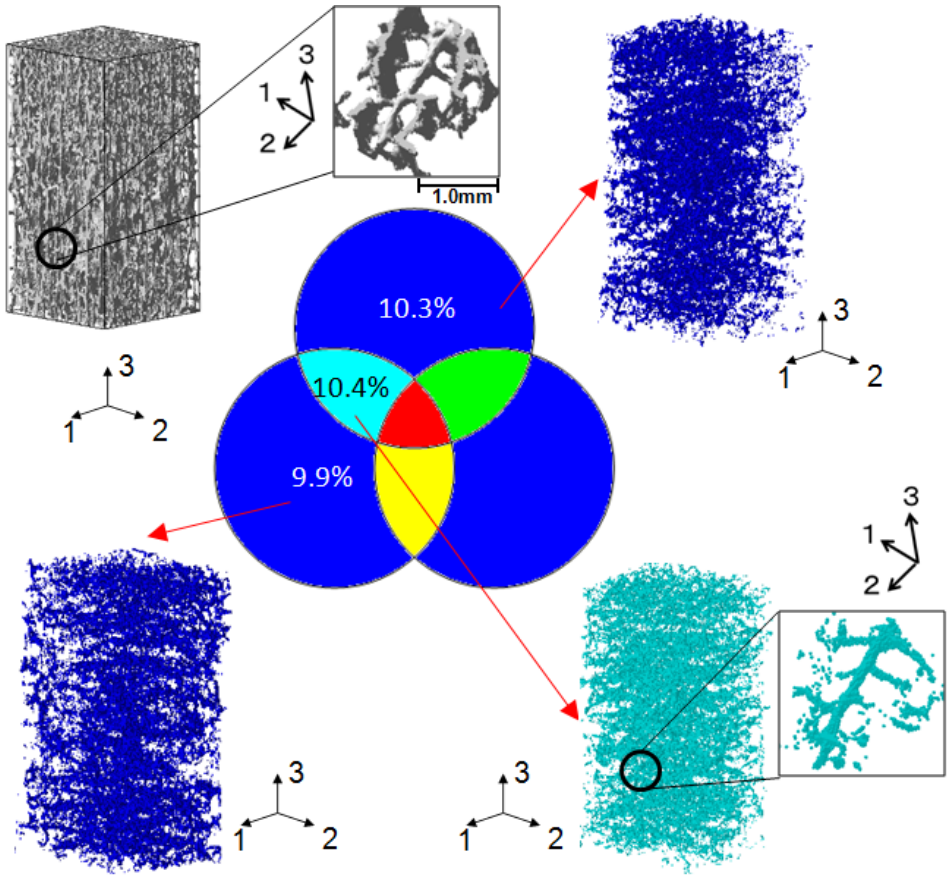

Fig. 10 Highlighted view of secondary trabeculae in healthy bone

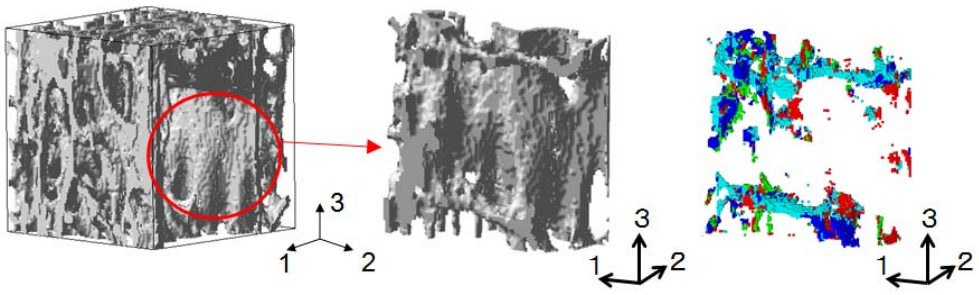

(a) ROI No. 2 and magnified view of plate-like bone (b) Compression in axis-1

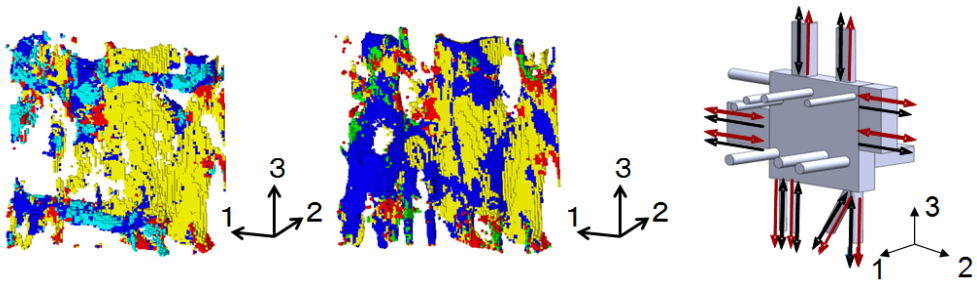

(c) Compression in axis-2 (d) Compression in axis-3 (e) Illustrative load path

Fig. 11 Classification of mechanical role of plate-like trabecular bone in ROI No. 2

4.2 Primary and secondary trabecular bone

The primary bone and the secondary bone were highlighted in very complex trabecular bone as shown in Figs. 8 to 10. Venn diagram in Fig. 7 implies that the primary bone mainly supports the self-weight, but half of the primary bone also works under compressive loads in left-right and post-ant directions. This is because those loads are distributed to the primary bone via plate-like trabecular bone as shown in Fig. 11(e). The secondary bone can be visualized as the load path used only for load in left-right or post-ant direction. However, the secondary bone was used as part of the load path network for all loading cases. From the comparison between the homogenized properties of healthy bone and osteoporotic bone implies that the secondary bone is dramatically decreased in osteoporotic bone.

4.3 Mechanical role of plate-like trabecular bone

The Venn diagrams obtained by ROI No. 1 (Fig. 7(a)) and No. 2 (Fig. 7(b)) show almost the same pattern of working voxels percentage. But they were different from the results obtained by ROI No. 3 (Fig. 7(c)) and ROI No. 4. The homogenized properties for No. 2 were higher than No. 1 because the bone density was higher due to the plate-like bone. While those for No. 3 and No. 4 were lower because they consist of rod-like bone only. The overall characteristics of trabecular bone in vertebra are expressed by the large ROI model No. 1. The above numerical results imply that the plate-like rich region dominates the overall characteristics of trabecular bone, and in other words, plate-like bone exerts a substantial influence on mechanical response of trabecular bone.

Fig. 11(e) implies that plate-like bone participates to the construction of a more effective network system. The number of plate-like trabecular bone, its area and the number of connected rod-like bone decrease in osteoporotic bone. It is supposed that plate-like bone plays the role of a hub. Network of trabeculae shows redundancy, so the load can pass through by using other way for healthy bone if some hub of the network is missing. However it is difficult to change the path for osteoporotic bone when some hub of network disappears because trabeculae for osteoporotic bone do not have much redundancy due to their morphology. The risk of fracture is then increased for osteoporotic bone.

The decrease of bone density leads to the stress concentration in rod-like trabecular bone. Comparison between Fig. 8(c) and 9(c), the length of the secondary bone, in other words, the distance between the primary bones is larger for osteoporotic bone than healthy bone. This may also lead to the stress concentration in secondary bone. Together with the stress concentration, the loss of the plate-like bone as a hub in load path network is supposed to raise the fracture risk of osteoporotic trabecular bone.

5. Conclusion

The homogenization method with finite element method was employed to analyze the microscopic trabecular bone in human lumbar vertebra taking into account BAp crystallite orientation. Comparison of the calculated macroscopic Young's modulus with the equation by Keyak et al. showed good agreement. Then, the macroscopic properties were examined in detail focusing on the anisotropy for osteoporotic bone. Since the homogenization method is advantageous in calculating the microscopic stress under variety of macroscopic loading conditions, a new post-processing technique was proposed to study the morphology and mechanical role of trabecular bone. The primary and secondary trabecular bone was clearly visualized with the load bearing functions against three basis loading conditions. The characteristic of plate-like bone was described by relating load path to network architecture.

Only two subjects were analyzed in this paper and more emphasis was put on the new post-processing methodology. In the next step, the number of subjects should be increased.

Other future works include stochastic analysis with uncertainty modeling of loading conditions and post-processing for dynamic analysis.

Acknowledgement

The authors would like to thank Prof. Yuji Nakajima and Prof. Hiroshi Kiyam (Osaka City University) for providing the bone specimen. Analysis of this bone specimen was approved by the Ethics Committee. We wish to thank the family of the donor for the generosity in the face of the bereavement.

The authors are grateful for the suggestions from Prof. Taiji Adachi (Kyoto University) for the development of the image-based homogenization software DoctorBQ used in this study, especially for anisotropic material modeling considering the BAp crystallite orientation. Also the dedicated help from Dr. Takuya Ishimoto and Dr. Sayaka Miyabe (both Osaka University) should be acknowledged. Part of this research was supported by Quint Corporation and Cybernet Systems Corporation.

Appendix A

To supplement the process flow in Fig. 1, the detailed algorithm to setup the anisotropic material axis, which was published in the authors' previous papers[10-11], is shown in the following flowchart. See also Appendix B for the explanation of axial direction of fourth lumbar to assume the self-weight load.

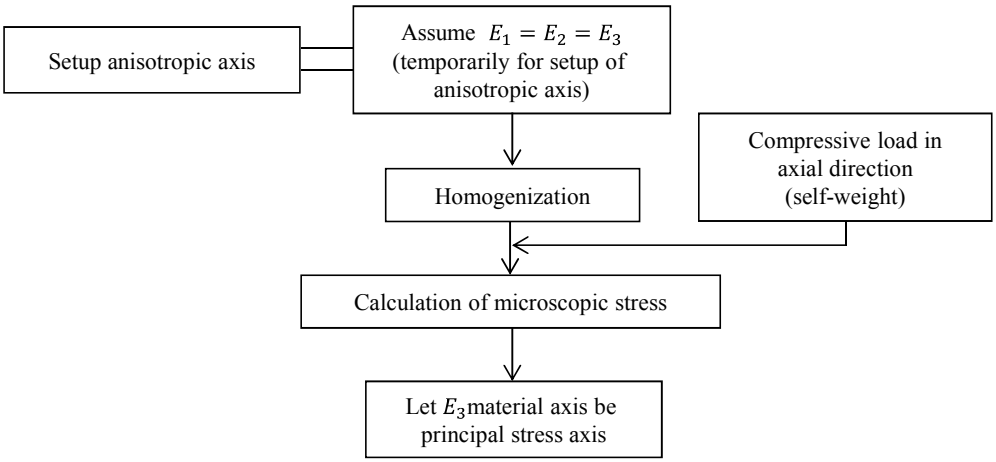

Fig. A.1 Detailed algorithm to setup anisotropic material axis

Appendix B

Fig. B.1 shows the transformation of the vertical axis for fourth lumbar (L4) from human body (spinal bone) to numerical model. The orientation of vertical axis (Axis-3) of numerical model is almost parallel to the vertical body axis.

Appendix C

In human vertebra of healthy bone, it is well known that the plate-like trabecular bone rich region is located in the middle part of lumbar, whilst the upper and lower parts consist of rod-like trabecular bone rich region, as shown in Fig. C.1(a). In osteoporotic bone, however, the plate-like bone is rarely seen even in the middle part of lumbar (Fig. C.1(b)). The typical plate-like trabecular bone is illustrated in Fig. C.1(c). It is found that rod-like trabecular bone is connected to plate-like trabecular bone.

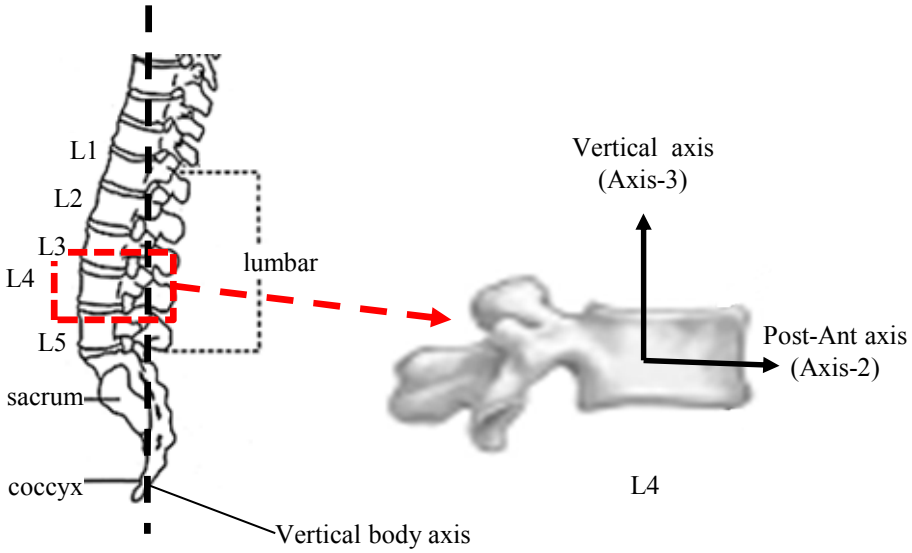

(a) Body axis of human body (b) Assumption of axes for L4 in numerical model

Fig. B.1 Transformation of vertical body axis

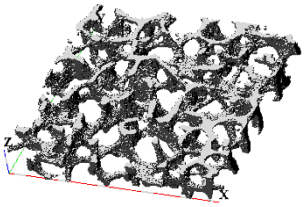

Lower and upper part
(rod-like trabecular bone rich region)

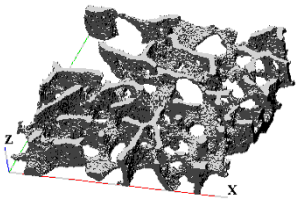

Middle part
(plate-like trabecular bone rich region)

(a) Healthy bone

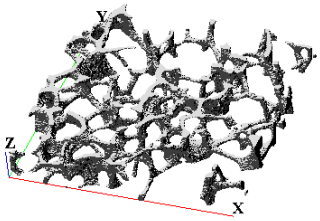

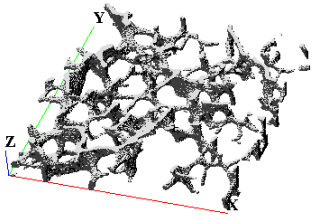

Middle part
(plate-like trabecular bone is rarely seen)

(b) Osteoporotic bone

(c) Illustration of typical plate-like trabecular bone

Fig. C.1 Plate-like and rod-like trabecular bone in human vertebra

References

(1) Ali, H., Rajit, A. and Sabhan, A., Validity of the DEXA diagnosis of involutional osteoporosis in patients with femoral neck fractures. *Indian Journal of Orthopaedics*, Vol. 44, No. 1 (2010), pp. 73-78.

(2) Bayraktar, H. and Keaveny, T., Mechanisms of uniformity of yield strains for trabecular bone. *Journal of Biomechanics*, Vol. 37 (2004), pp. 1671-1678.

(3) Nagaraja, S., Couse, T. and Guldberg, R., Trabecular bone microdamage and microstructural stresses under uniaxial compression. *Journal of Biomechanics*, Vol. 38 (2005), pp. 707-716.

(4) Kleerekoper, M., Villanueva, A. R, Stanciu, J., Rao, D. and Parfitt, A. M., The role of three-dimensional trabecular microstructure in the pathogenesis of vertebral compression fractures. *Calcified Tissue International*, Vol. 37 (1985), pp. 594–597.

(5) Carter, D., Orr, T. and Fyhrie, D., Relationships between loading history and femoral cancellous bone architecture. *Journal of Biomechanics*, Vol. 22 (1989), pp. 231–44.

(6) Weinans, H., Huiskes, R. and Grootenboer, H.J., The behavior of adaptive bone-remodeling simulation models. *Journal of Biomechanics*, Vol. 25 (1992), pp. 1425–41.

(7) Adachi, T., Suzuki, Y., Tsubota, K. and Hojo, M., Computer simulation of trabecular remodeling in human proximal femur using large-scale voxel finite element models. *Journal of Japanese Society of Bone Morphometry*, Vol. 17, No. 3 (2007), pp. 15-20. (in Japanese)

(8) Nakano, T., Kaibara, K., Tabata, Y., Nagata, N., Enomoto, S., Marukawa, E. and Umakoshi, Y., Unique alignment and texture of biological apatite crystallites in typical calcified tissues analyzed by microbeam x-ray diffractometer system. *Bone*, Vol. 31, No. 4 (2002), pp. 479-487.

(9) Miyabe, S., Ishimoto, T. and Nakano, T., Preferential orientation of biological apatite in normal and osteoporotic human vertebral trabeculae. *Journal of Physics: Conference Series*, Vol. 165 (2009), doi:10.1088/1742-6596/165/1/012087.

(10) Kawagai, M., Takano, N., Nakano, T. and Asai, M., Multi-Scale Stress Analysis of Trabecular Bone Considering Trabeculae Morphology and Biological Apatite Crystallite Orientation. *Journal of the Society of Materials Science*, Vol. 55, No. 9 (2006), pp. 874-880. (in Japanese)

(11) Tawara, D., Adachi, T., Takano, N. and Nakano, T., High resolution micro-mechanical analysis of cancellous bone in vertebra considering bone quality. *Japanese Journal of Clinical Biomechanics*, Vol. 29 (2008), pp. 7-14. (in Japanese)

(12) Lions, J. L., Some methods in the mathematical analysis of systems and their control. (1981), Science Press Beijing.

(13) Hollister, S.J., Brennan, J. M. and Kikuchi, N., A homogenization sampling procedure for calculating trabecular bone effective stiffness and tissue level stress. *Journal of Biomechanics*, Vol. 27, No. 4 (1994), pp. 433-444.

(14) Kosturski, N. and Margenov, S., Numerical Homogenization of Bone Microstructure, *Large-Scale Scientific Computing*. (2010), p. 140–147, Springer-Verleg Berlin Heidelberg.

(15) Rietbergen, B., Majumdar, S., Pistoia, W., Newitt, C., Kothari, M., Laib, A. and Ruegsegger, P., Assessment of cancellous bone mechanical properties from micro-FE models based on micro-CT, pQCT and MR images. *Technology and Health Care*, Vol. 7 (1998), pp. 413-420.

(16) Keyak, J. H., Lee, I. Y. and Skinner H. B., Correlations between orthogonal mechanical properties and density of trabecular bone: Use of different densitometric measures. *Journal of Biomedical Materials Research*, Vol. 28 (1994), pp. 1329-1336.

(17) Keller T., Predicting the Compressive Mechanical Behavior of Bone. *Journal of*

Biomechanics, Vol. 27, No. 9 (1994), pp. 1159-1168.

(18) Carter, D. and Hayes, W., The compressive behavior of bone as a two-phase porous structure. *The Journal of Bone and Joint Surgery*, Vol. 59, No. 7 (1977), pp. 954-962.

(19) Takano, N., Uetsuji, Y. and Asai, M., Micro mechanical simulation. (2008), p. 130. Corona Publishing. (in Japanese)

(20) Takano, N., Zako, M., Kubo, F. and Kimura, K., Microstructure-based stress analysis and evaluation for porous ceramics by homogenization method with digital image-based modeling. *International Journal of Solids and Structures*, Vol. 40 (2003), pp. 1225-1242.

(21) Takano, N., Fukasawa, K. and Nishiyabu, K., Structural strength prediction for porous titanium based on micro-stress concentration by micro-CT image-based multiscale simulation. *International Journal of Mechanical Sciences*, Vol. 52 (2010), pp. 229-235.

(22) Tawara, D., Takano, N., Adachi, T. and Nakano, T., Mechanical evaluation of trabecular bone of human vertebra based on multi-scale stress analysis. *Journal of Japanese Society for Bone Morphometry*, Vol. 20, No. 1 (2010), pp. 100-107. (in Japanese)